PROCEEDINGS A

royalsocietypublishing.org/journal/rspa

Research

Cite this article: O'Kiely D, Xin M, Lecointre P, Vella D. 2025 Wrinkling of a bilayer with spatially varying stiffness: from wrinkle branching to cascades. *Proc. R. Soc. A* **481**: 20240842.
https://doi.org/10.1098/rspa.2024.0842

Received: 1 November 2024
Accepted: 2 May 2025

Subject Areas:
applied mathematics, mechanics

Keywords:
wrinkling, pattern formation, bifurcation theory

Author for correspondence:
Dominic Vella
e-mail: dominic.vella@maths.ox.ac.uk

Wrinkling of a bilayer with spatially varying stiffness: from wrinkle branching to cascades

Doireann O'Kiely[1,2], Meng Xin[3], Paul Lecointre[2] and Dominic Vella[2]

[1]Mathematics Applications Consortium for Science and Industry (MACSI), Department of Mathematics and Statistics, University of Limerick, Limerick V94 T9PX, Ireland
[2]Mathematical Institute, University of Oxford, Woodstock Road, Oxford OX2 6GG, UK
[3]Department of Physics, University of Massachusetts, Amherst, MA 01003, USA

DV, 0000-0003-1341-8863

We consider the problem of elastic wrinkling for the case where the energetically favourable wrinkle number (or wavelength) varies in space. Ordinarily, such changes are believed to take place via a 'wrinkle cascade' in which individual wrinkles break into two (or more) wrinkles all at the same location: many wrinkles are introduced at a single location, and away from this location the wrinkle pattern appears mono-chromatic, with a single mode dominating the pattern at each location. We show that it is also possible for wrinkles to be added gradually, via a small subset of wrinkles branching repeatedly. In this 'wrinkle branching' regime, the wrinkle pattern is polychromatic, with several modes dominating the pattern at each location. Using a combination of numerical simulations, analysis and experiments, we show that this wrinkle branching mode is observed when the rate of change of preferred wrinkle number is sufficiently slow. We note that in this regime the branching occurs where the wrinkle amplitude is smallest, making it difficult to observe experimentally, and speculate that this may explain why it appears not to have been often reported before.

Electronic supplementary material is available online at https://doi.org/10.6084/m9.figshare.c.7834474.

THE ROYAL SOCIETY PUBLISHING

1. Introduction

Wrinkles occur in a plethora of situations involving thin sheets coating a deep substrate and are ubiquitous in our everyday lives (human skin, stretched plastic wrapping) as well as being used in technological settings (including photovoltaics [1] and optical gratings [2] for example). Desire to understand and control wrinkling patterns has motivated the development over the last 20 years of a framework for describing and predicting wrinkle patterns [3–6]. The starting point of this theory is to understand how the essential ingredients for wrinkling—in-plane compression and an energetic penalty to out-of-plane deformation at the system scale—interact to select a wrinkle wavelength.

To understand why an interaction between compression and an energetic penalty is needed, note that a thin sheet subject to in-plane compression buckles at the largest scale available to it (think of compressing a piece of card using your hands). However, if the sheet is attached to a substrate (e.g. another elastic body or a liquid), this substrate resists out-of-plane motion, preferring highly convoluted, but small-amplitude, wrinkles to form. A balance between the sheet's desire to adopt the largest wavelength possible and the substrate's preference for small amplitudes leads to the formation of many wrinkles at an intermediate, emergent length scale [7]. This length scale is the energetically preferred one but, in general, differs from the wrinkle wavelength close to onset, which is determined by linear stability analysis close to the buckling threshold; this energetic structure is the basis of the Far from Threshold theory of wrinkling [3,4,6].

An analogous minimization of the combination of a sheet's bending energy and an energetic penalty from an effective substrate can be performed when, in the direction along the wrinkles, a buckled sheet is curved [7,8] or subject to a tension [3]. Paulsen *et al.* [7] used this analogy for different influences to propose a 'local λ-law', stating that the energetically optimal wrinkle wavelength for a sheet with bending stiffness B is

$$\lambda = 2\pi \left(\frac{B}{K_{\mathrm{sub}}(x)} \right)^{1/4}, \tag{1.1}$$

where $K_{\mathrm{sub}}(x)$ is the local value of the total substrate stiffness that combines the effects of 'real' stiffness with the effects of curvature and applied tension.

The form of equation (1.1) has been considered in prototypical problems of interest including uniaxial compression of a rectangular elastic sheet on a soft elastic substrate [9], indentation of a floating elastic sheet [7,10,11] and the confinement of an elastic sheet between geometrically incompatible shells [12]. However, the expression in equation (1.1) glosses over the fact that the wrinkle wavelength is required to change for non-uniform K_{sub}, which will, in general, require the birth of new wrinkles. It has been found that equation (1.1) gives a good account of the results of experiments [7] and numerical simulations [6] provided that the spatial variation of the wrinkle wavelength is in some sense 'slow'. Moreover, even for a uniform K_{sub}, geometry may necessitate the birth of new wrinkles—for example, a circular geometry is incompatible with a constant preferred wavelength [12]. The birth of new wrinkles has been studied in several idealized settings with the fundamental ingredient through which a single new wrinkle is born, often termed a 'wrinklon' [13–15].

Previous experiments have illustrated three general causes of a variation in the wrinkle number or wavelength, with examples shown in figure 1: (i) when material properties vary in space (figure 1a,c), (ii) when the amplitude of wrinkles is suppressed near a boundary (figure 1a,b), and (iii) in axisymmetric scenarios, when radial wrinkles on a circular sheet must multiply to maintain an (approximately) constant wavelength (e.g. figure 1d).

The requirement that wrinkle wavelength varies 'slowly' enough for equation (1.1) to apply typically includes variations of types (i) and (iii) above, even when the amplitude is modulated at a different frequency [12]. However, attempts to rationalize wrinkle evolution of type (ii) theoretically have led to the concepts of wrinklons [14,15] and cascades [17]. Vandeparre *et al.* [15] described a wrinklon as 'the localized transition zone in the merging of two wrinkles', and characterize its size and amplitude [21]. Davidovitch and co-authors investigated cascades, in

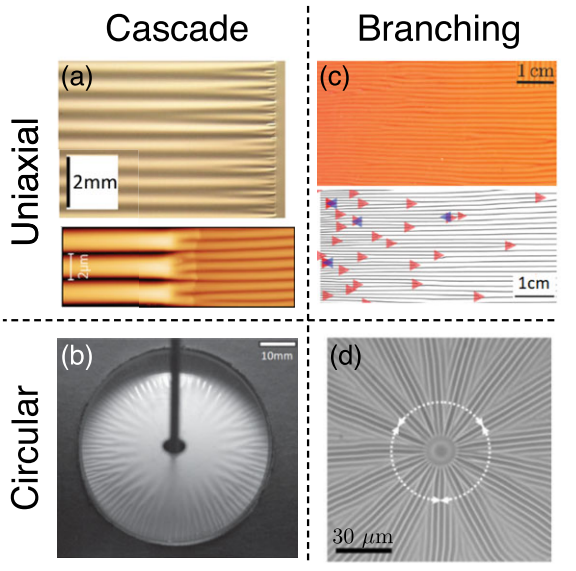

Figure 1. Examples of the spatial evolution of wrinkle patterns observed in previously reported experiments: (a) and (b) show step-like changes in wavelength—a cascade. In (a) wrinkles are generated by a lateral tension and orthogonal compression while in (b) a planar sheet is confined in the gap between two spherical shells. Figures reproduced from: (a) bottom [16] (with permission from the Royal Society of Chemistry), top [17] (with permission from the American Physical Society) and (b) [18] (with permission from the American Physical Society); (c) and (d) show wrinkle branching for two systems: (c) a beam (of smoothly varying thickness) attached to a uniform substrate and subject to compression (used with permission of Royal Society of Chemistry, from [19]; permission conveyed through Copyright Clearance Center, Inc.) and (d) a circular geometry with wrinkling caused by swelling of the sheet in a central circular region (reproduced from [20], with permission from Wiley).

which a coarse wrinkle structure in the bulk of a sheet becomes ever finer near a constrained edge [13,17]. Each of these ingredients successfully describes a different aspect of wrinkle branching, namely stress localization near the branching event, global patterns of successive branching events and stress alleviation in the vicinity of a branching event.

Tension plays a significant role in the scenarios outlined above; Davidovitch [13] suggested that smooth profiles should be anticipated even in evolving wrinkle patterns provided that the tension $T \gtrapprox \sqrt{BK_{\mathrm{sub}}}$, but that folds should be expected below this threshold. When folds or other localized structures do occur, a rich variety of patterns are possible, see e.g. [22]. In the case of buckling near a clamped edge where the system must adjust from some global profile to the smallest allowed wavelength near the buckling edge, wavelength adjustment is typically observed to take the form of a cascade [13–15,17,23]. In the absence of tension, Pomeau [23] predicted a cascade of folds, while for moderate tension Vandeparre *et al.* [15] predicted that smoothing would give rise to a cascade of wrinkles. Huang *et al.* [17] postulate that individual branching events within the cascade will be stretched out by increasing the tension, while Vandeparre *et al.* [15] found that the length $\mathcal{L}$ of wrinklons should increase with tension and decrease with substrate stiffness according to

$$\mathcal{L}(\lambda) = \frac{\lambda^2}{h}\sqrt{\frac{T}{Eh}} \propto \sqrt{\frac{T}{K_{\mathrm{sub}}(x_*)}}, \tag{1.2}$$

where h and E are the thickness and Young's modulus of the sheet, respectively. We note that although many experiments reported in the literature do not have an applied tension (including some of those in figure 1), deformation of the sheet and substrate is likely to induce a tension, which may explain the occurrence of smooth branching profiles.

In this paper, we attempt to unify the different wrinkle evolution phenomenologies outlined above by studying the simplest possible wrinkle evolution scenario: uniaxial compression of a

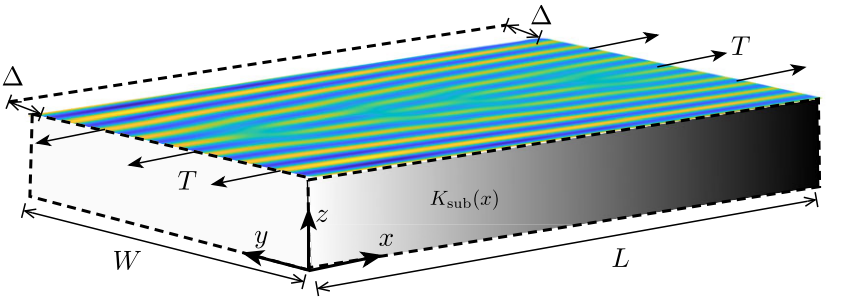

Figure 2. Schematic of the setup of a sheet subject to a longitudinal tension T and an orthogonal compression Δ. The sheet lies on a linear substrate whose stiffness, $K_{\mathrm{sub}}(x)$, varies with position along the tensile axis.

thin, rectangular elastic sheet on a soft elastic substrate, whose stiffness varies spatially. We begin by simulating the system in Surface Evolver, and our results, analysis and insights are presented in §2. We then proceed to a more fundamental mathematical investigation, where we study the evolution of individual Fourier modes in the wrinkle profile. Our analysis and the outcomes are presented in §3, which leads to a qualitative comparison to experiment (§4) and more detailed analysis (§5). Finally, we discuss our findings and their implications in §6.

2. Surface Evolver simulations

We use Surface Evolver simulations as a first tool to understand how changes in preferred wrinkle wavelength are accommodated by the sheet [24,25].

(a) Model problem

We consider a rectangular elastic sheet of bending stiffness B, adhered to a soft substrate with stiffness K_{sub}. We denote the length of the system by L and its width by W. We allow the substrate stiffness to vary in the x-direction, so that $K_{\mathrm{sub}} = K_{\mathrm{sub}}(x)$ as illustrated in figure 2. We apply a tension T in the x-direction at the same time as imposing an end—shortening in the y-direction by displacing the sheet edge from $y = W$ to $y = W - \Delta$. We realize this scenario in Surface Evolver by minimizing the total energy contributed by stretching and bending of the sheet and deformation of the substrate. Details of the implementation may be found in the electronic supplementary material.

In the *absence* of spatial variation, the locally preferred wavelength [7] in the wrinkled sheet would be given by

$$\lambda_{\mathrm{loc}} = 2\pi \left(\frac{B}{K_{\mathrm{sub}}}\right)^{1/4}. \tag{2.1}$$

With a spatially varying substrate stiffness $K_{\mathrm{sub}}(x)$, we choose the spatial variation in such a way that the locally preferred wavelength varies linearly in space according to

$$\lambda_{\mathrm{loc}} = \frac{W}{n_0} + \left(\frac{W}{n_L} - \frac{W}{n_0}\right)\frac{x}{L}, \tag{2.2}$$

with n_0 and n_L desired (preferred) numbers of wrinkles at $x = 0$ and $x = L$, respectively.

We anticipate that the number of wrinkles observed in the sheet will evolve in tandem with the change in 'preferred' wavelength, which will require wrinkle branching or the appearance of new wrinkles. The exact nature of the evolution will depend on the steepness of the stiffness gradient and on the tension in the sheet. According to Davidovitch [13], irregular cascades formed of sharp folds occur in the limit $T \to 0$, while a smooth shape can be expected for $T \gtrsim \sqrt{BK_*}$. In this paper, we focus on the case $T \gtrsim \sqrt{BK_*}$ only, and the Surface Evolver simulations presented in this

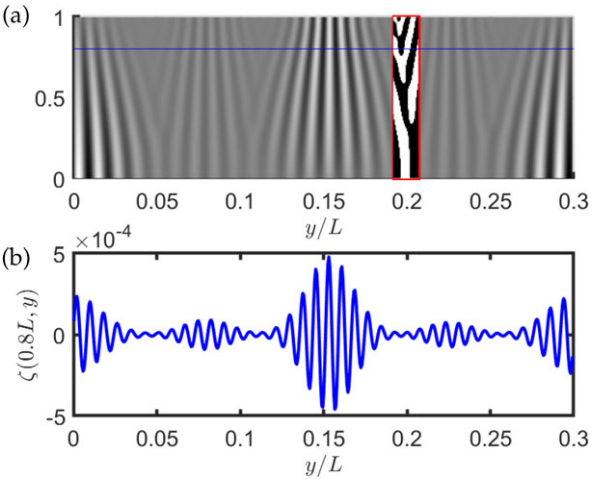

Figure 3. (a) Surface Evolver simulations for a sheet with a confinement $\Delta/W = 3.9 \times 10^{-4}$ on a substrate with spatially varying stiffness chosen such that the locally preferred number of wrinkles varies from $n_0 = 24$ to $n_L = 48$ via equation (2.2). The overlaid inset, centred at $y/L = 0.2$, is colour-saturated to show a line of defects more clearly. (b) Surface height ζ at position $x/L = 0.8$ (indicated by the horizontal blue line in (a)). The Poisson ratio $\nu = 0.4$, the units of Young's modulus and thickness are chosen so that $Eh = 1$, and no tension is applied at the boundaries $x/L = 0, 1$.

section satisfy $T \gg \sqrt{BK_*}$ and $|\mathrm{d}(B/K_{\mathrm{sub}})^{1/4}/\mathrm{d}x| \ll 1$. Our Surface Evolver simulations use a small compression, Δ, to minimize the likelihood of folds forming (see section S1.2 of the electronic supplementary material). We briefly discuss the possibility of exceeding the wrinkle-to-fold threshold in §6.

(b) Amplitude modulation

Typical results from our Surface Evolver simulations are shown in figure 3. This shows a system in which the preferred number of wrinkles varies from $n_0 = 24$ to $n_L = 48$, following equation (2.2), for a sheet with aspect ratio $W/L = 0.3$. In this example, we see that branching events appear to have aligned in space, so that they occur along lines $y \approx \mathrm{cst}$ (e.g. $y/L \approx 0.2$). In conjunction with this, we observe amplitude modulation in the system, i.e. the wrinkle amplitude is suppressed in the vicinity of branching events. This is consistent with previous predictions by Tovkach *et al.* [12] in the context of wrinkle-branching caused by geometric incompatibility. Although this is a valuable qualitative observation, we require further analysis to make quantitative observations of the wrinkle wavelength as a function of space. We achieve this in §2(c) by carrying out a Fourier transform of the wrinkle profiles determined numerically using Surface Evolver for different parameter choices. The Surface Evolver simulations are relatively computationally intensive, so to enable this deeper examination of how the wrinkle profiles are affected by parameters we consider narrower sheets in the y-direction and impose periodic boundary conditions. This means the spacing of branching lines in the y-direction is prescribed, but the wavelength evolution in the x-direction can still be investigated.

(c) Wrinkle selection

In figure 4, we show that tension has a dramatic effect on the visual appearance of spatially varying wrinkles. In each of the three panels, the 'preferred' number of wrinkles increases smoothly from $n_0 = 3$ to $n_L = 24$ via equation (2.2), and the actual number of wrinkles increases through branching events. These branching events occur at approximately the same value of x in each case, but the branching events become more elongated as tension increases; this is consistent with the square-root dependence of wrinklons on tension predicted by Vandeparre *et al.* [15], see

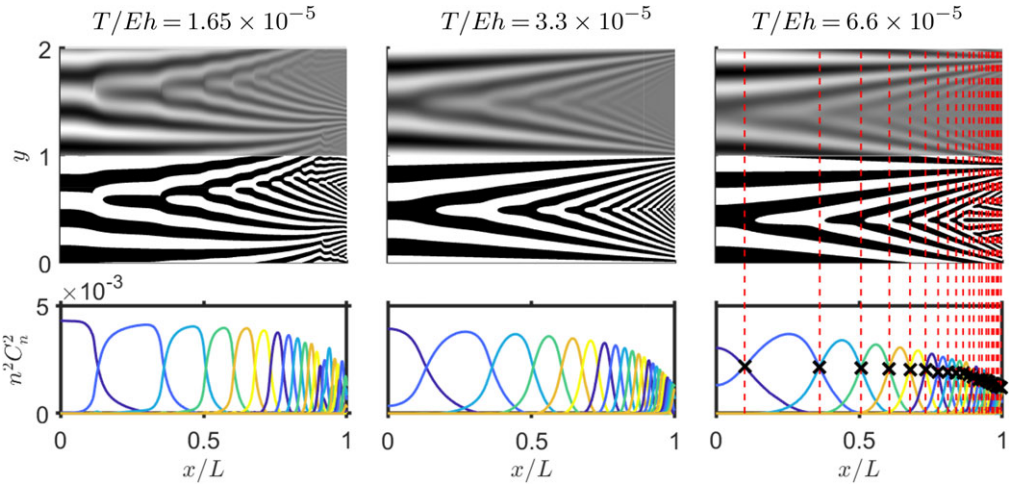

Figure 4. Surface Evolver simulations for a sheet of width $W/h = 1.6 \times 10^4$ and length $L/W = 15.4$ and Poisson's ratio $\nu = 0.4$, subject to a confinement $\Delta/W = -0.0016$ for three different tensions $T/Eh = 1.65 \times 10^{-5}$ (left), $T/Eh = 3.3 \times 10^{-5}$ (centre) and $T/Eh = 6.6 \times 10^{-5}$ (right). The sheet is adhered to a spatially varying substrate whose stiffness causes the locally preferred wrinkle number to increase from 3 to 24 over the length L. In the top panel, the actual surface profile is shown. Below it, the profile is saturated to show the wrinkle branching more clearly. The bottom panel shows the scaled amplitude C_n of Fourier modes corresponding to $n = 3, 4, \ldots 24$. In the last panel, the black crosses and red vertical dashed lines mark the x-values at which values of $n^2C_n^2$ cross.

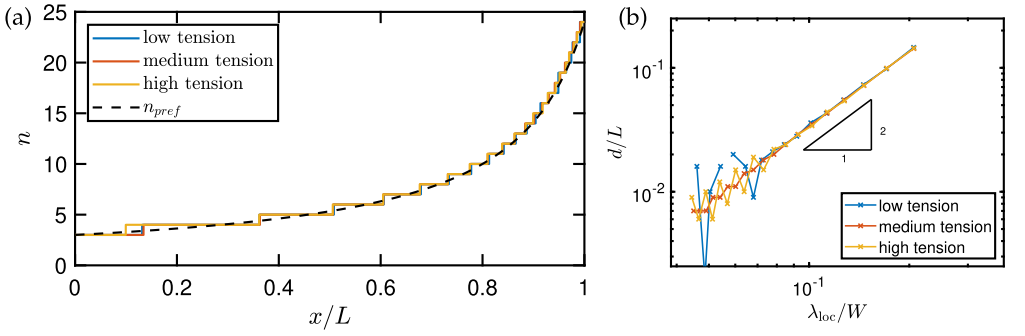

Figure 5. (a) Dominant wavenumber measurements for the three cases studied in figure 4. Coloured lines show the Surface Evolver prediction of the dominant wavenumber, defined as the Fourier mode with maximum amplitude. The dashed black line shows the locally preferred wavenumber $n_{\text{pref}} = W/\lambda_{\text{loc}}$, with λ_{loc} as in equation (2.2). (b) Distance d between defects as a function of λ_{loc}, which varies in space. The tension values are $T/Eh = 1.65 \times 10^{-5}$ (blue, low tension), $T/Eh = 3.3 \times 10^{-5}$ (red, medium tension) and $T/Eh = 6.6 \times 10^{-5}$ (yellow, high tension). The results contain some numerical noise, which increases with decreasing T.

equation (1.2). We investigate this in more detail by decomposing the wrinkle profile into Fourier modes. We see that all of the modes between 3 and 24 are excited at some point in the interval $x \in [0, L]$. The amplitudes peak locally as the substrate stiffness evolves spatially. We can extract the 'dominant' mode by identifying the Fourier mode with the largest amplitude at each value of x, and we confirm that this is well aligned with the locally preferred number of wrinkles in figure 5a, at least in the regime for which $|\mathrm{d}(B/K_{\text{sub}})^{1/4}/\mathrm{d}x| \ll 1$, $T \gg \sqrt{BK_*}$ simulated here. This behaviour also manifests in the distance d between defects in the pattern, as shown in figure 5b: based solely on the underlying preferred wrinkle wavelength profile, we would expect d to be

such that $n_{\mathrm{pref}}(x_* + d) - n_{\mathrm{pref}}(x_*) = 1$. Taylor expanding this expression to first order in d we find that $d = 1/|n'_{\mathrm{pref}}(x_*)| = \lambda_{\mathrm{loc}}^2/(W|\lambda'|)$, which is independent of the applied tension, T/Eh, and hence qualitatively different to the wrinklon scaling equation (1.2). Figure 5b shows that the spacing between branching events is independent of tension (except for some numerical noise at small tension) in our simulations. However, figure 4 shows that the shape of the amplitude profiles *does* change as the tension changes: when the tension is small the change of amplitude of each mode is almost-step-like but becomes smoother as the tension increases.

3. Mathematical analysis

Following on from the Fourier decomposition of our Surface Evolver simulations in figures 4 and 5 we now proceed to investigate and explain the observed phenomena from a theoretical viewpoint. Our starting point is the fully nonlinear Föppl–von Kármán equations for the vertical displacement of the sheet, $\zeta(x, y)$. We then decompose these governing equations to see what further insights we can gain.

(a) Governing equations

Our starting point is the first Föppl–von Kármán equation for the out-of-plane displacement $\zeta(x, y)$ of a rectangular sheet of length L, width W and bending stiffness B. The sheet is subject to a vertical restoring force from the linear (Winkler) substrate of stiffness $K_{\mathrm{sub}}(x)$. The full equation is

$$B\nabla^4\zeta - \boldsymbol{\sigma} : \nabla\nabla\zeta + K_{\mathrm{sub}}(x)\zeta = 0. \tag{3.1}$$

To make analytical progress, this equation requires some simplification. We assume that the wrinkle wavelength and amplitude are small compared with other lengthscales; in this limit, we expect that $B\nabla^4\zeta \approx B\partial^4\zeta/\partial y^4$. Turning our attention to the stress term, we note that in-plane stress equilibrium, $\nabla \cdot \boldsymbol{\sigma} = 0$ can be satisfied by $\sigma_{xx} = T$, $\sigma_{xy} = 0$ and $\sigma_{yy} = \sigma_{yy}(x)$. We therefore approximate the out-of-plane force balance (equation (3.1)) by

$$B\frac{\partial^4\zeta}{\partial y^4} - T\frac{\partial^2\zeta}{\partial x^2} - \sigma_{yy}\frac{\partial^2\zeta}{\partial y^2} + K_{\mathrm{sub}}(x)\zeta = 0. \tag{3.2}$$

Note that in equation (3.2), σ_{yy} is unknown but may be interpreted as a Lagrange multiplier associated with the imposed compression $\Delta > 0$. Assuming small strain, i.e. $\epsilon_{yy} = \sigma_{yy}/(Eh) \ll 1$, we have that

$$\frac{1}{2}\int_0^W \left(\frac{\partial\zeta}{\partial y}\right)^2 \mathrm{d}y = \Delta. \tag{3.3}$$

We further consider the limit in which the preferred wavelength λ_{pref} is much smaller than the channel width, W. Since $\lambda_{\mathrm{pref}} = 2\pi(B/K_*)^{1/4}$, where $K_* = K_{\mathrm{sub}}(x_*)$ is the substrate stiffness at a particular position $x = x_*$, the preferred number of wrinkles $n_* = n_{\mathrm{pref}}(x_*) = W/\lambda_{\mathrm{pref}} \gg 1$ and we consider the limit

$$\delta = 2\pi\left(\frac{B}{K_* W^4}\right)^{1/4} = \frac{1}{n_*} \to 0. \tag{3.4}$$

In this limit, we anticipate that $\sigma_{yy}(x)$ will be close to $-2\sqrt{BK_{\mathrm{sub}}(x)}$, the expected value for a uniform-substrate with the same local stiffness [12]. We therefore introduce a dimensionless residual compressive stress S, which is defined by

$$\sigma_{yy}(x) = \sqrt{BK_{\mathrm{sub}}(x)}(-2 + S). \tag{3.5}$$

To make further progress, we assume that the deflection $\zeta(x, y)$ may be decomposed into Fourier modes

$$\zeta(x, y) = \sum_n C_n(x)\sin\left(2\pi n\frac{y}{W} + \beta_n\right). \tag{3.6}$$

Our task is then to determine the amplitude of each mode as a function of x, $C_n(x)$, as well as the behaviour of the residual compressive stress $S(x)$. (We have included a phase shift β_n for each

mode for generality.) We note that this approach is only valid in the regime $T \gtrsim \sqrt{BK_*}$, when we expect a smooth surface profile even in regions where the number of wrinkles changes [13]. Note that we will restrict n to integer values in this analysis, so that ζ is periodic on $y \in [0, W]$ in line with the Surface Evolver simulations of §2.

Substitution of the decomposition (equation (3.6)) into the governing equation (3.2) together with the transverse stress from equation (3.5) yields the second-order evolution equations for the amplitudes $\{C_n\}$:

$$T\frac{\mathrm{d}^2 C_n}{\mathrm{d}x^2} = K_*\delta^4\left\{\left[n^2 - n_{\mathrm{pref}}(x)^2\right]^2 + n^2 n_{\mathrm{pref}}(x)^2 S\right\} C_n. \tag{3.7}$$

The unknown function $S(x)$ must then be determined from the integral constraint (equation (3.3)), which leads to the constraint

$$\Delta W = \pi^2 \sum_n n^2 C_n^2. \tag{3.8}$$

The tension $T \neq 0$ must be known for equations (3.7) and (3.8) to fully determine S and the amplitudes $\{C_n\}$.

We note that the number of wrinkles observed at a particular x changes only slowly, and by an integer number. Hence, if we consider a domain over which the wavenumber of wrinkling changes by an order one amount, i.e. the number of wrinkles at the end $n_{\mathrm{end}} = n_* + \Delta n = O(1/\delta)$, where $\Delta n = O(1)$, then we can usefully write any $n = n_*(1 + \delta \cdot j)$ for some $O(1)$ integer j. In this way, j measures how far from n_* we have ventured and can be chosen to be some convenient index. This will be particularly useful in the limit $\delta \to 0$ that we consider.

The discrete constraint (equation (3.8)) suggests introducing a rescaled mode amplitude $Z_j = \pi n_j C_{n_j}/\sqrt{\Delta W}$, while the modal FvK equation (3.7) suggests introducing a scaled x-coordinate $\bar{X} = \delta(x - x_*)/\sqrt{T/K_*}$. With these rescalings and taking the limit $\delta \to 0$ equations (3.7) and (3.8) lead to

$$\frac{\mathrm{d}^2 Z_j}{\mathrm{d}\bar{X}^2} = F_j(\bar{X})Z_j + \bar{S}Z_j \tag{3.9a}$$

and

$$\sum_j Z_j^2 = 1, \tag{3.9b}$$

where

$$F_j(\bar{X}) = 4(\kappa - \kappa_j)^2, \tag{3.10}$$

and we let $\bar{S} = S/\delta^2$ to ensure that the various terms remain $O(1)$ as $\delta \to 0$. Here, we have introduced scaled versions of the preferred and observed wavenumbers defined by $\kappa(\bar{X}) = n_{\mathrm{pref}}(x) - n_*$ and $\kappa_j = n_j - n_*$, respectively; note that $\kappa(\bar{X})$ and κ_j are both $O(1)$. We also note that the length scaling used here differs from the wrinklon length defined by Vandeparre *et al.* [15], see equation (1.2), by a factor $1/\delta$; we will explain this difference in §3(b).

We interpret equation (3.9) as a system of $N+1$ equations for N amplitudes $\{Z_j\}$ and an unknown stress contribution S, which can be solved in conjunction with suitable boundary conditions to yield the wrinkle profile in the sheet. Numerical solution is complicated by the fact that equation (3.9) is a differential-algebraic system because of the constraint in equation (3.9*b*). We handle this by representing the N-tuple $\{Z_1, Z_2, \ldots, Z_N\}$ as a point on the $(N-1)$-sphere [26], thereby reducing the number of variables by one and ensuring that the constraint is automatically satisfied. We now digress briefly to illustrate this method for the simplest case: $N = 2$.

Example 3.1 (Constraint handling for $N = 2$). With two modes only, we let $Z_1 = \cos\theta$, $Z_2 = \sin\theta$ for some $\theta(X)$. After some straightforward manipulations, we find that:

$$\frac{\mathrm{d}^2\theta}{\mathrm{d}\bar{X}^2} = \frac{F_2 - F_1}{2}\sin 2\theta, \tag{3.11}$$

with boundary conditions $\theta \to 0$ as $\bar{X} \to -\infty$, $\theta \to \pi/2$ as $\bar{X} \to +\infty$ and $\bar{S}$ given explicitly as

$$\bar{S} = -\left(\frac{\mathrm{d}\theta}{\mathrm{d}\bar{X}}\right)^2 - F_1 - F_2. \tag{3.12}$$

This method of handling the constraint (equation (3.9*b*)) can be generalized for larger values of N by introducing further angles, θ_i. Below, we focus on the case $N=5$, for which details of the representation in terms of the set $\{\theta_i; 1 \le i \le 4\}$ and the eighth-order system to be solved (four second-order equations) are given in the electronic supplementary material. The important outcome of this procedure is that, in the limit $\delta \to 0$, we can first solve a system of ordinary differential equations to determine the amplitudes, $\{Z_j\}$, and then determine the stress perturbation, $\bar{S}$, *a posteriori*. Validation of our methodology may also be found in the electronic supplementary material.

(b) Effect of stiffness gradient

We investigate the influence of the stiffness gradient on wrinkle branching by solving the model problem outlined above. In particular, we consider a sample problem in which the preferred wavenumber changes by 5 within the domain of interest, i.e. we consider the case $N=5$ of equations (3.9) and (3.10). To consider the effect of the stiffness gradient, we take the particular stiffness profile

$$n_{\text{pref}} - n_* = \kappa(\bar{X}) = 2\tanh(\alpha \bar{X}), \tag{3.13}$$

so that α is the dimensionless parameter characterizing the stiffness gradient. Redimensionalizing and differentiating, we can write α in various different forms

$$\alpha = \frac{1}{8\delta^2}\frac{K_{\text{sub}}'(x_*)}{K_{\text{sub}}(x_*)}\sqrt{\frac{T}{K_{\text{sub}}(x_*)}} = \frac{1}{16\pi\delta}\frac{K_{\text{sub}}'(x_*)}{K_{\text{sub}}(x_*)/W}\sqrt{\frac{T}{\sqrt{BK_{\text{sub}}(x_*)}}} = \frac{1}{32\pi^2}\frac{W^2}{\ell_{bc}\ell_k}, \tag{3.14}$$

where $\ell_{bc} = (B/T)^{1/2}$ is the bendocapillary length and $\ell_k = K(x_0)/K'(x_0)$ is the length scale over which the substrate stiffness varies. We can therefore interpret α as a measure of both the steepness of the substrate gradient and the strength of tension: when α is small, the substrate stiffness changes slowly in space (or tension is weak), while large α corresponds to a steep gradient (or strong tension).[1]

We also note that α increases with $K_{\text{sub}}'(x_*)$: bigger relative changes in wavelength or preferred wrinkle number should actually correspond to shorter individual branching events. This explains the somewhat counterintuitive fact that the defects in this paper, which are required to induce an $O(\delta)$ change in wrinkle number, are a factor $1/\delta$ longer than the wrinklons studied by Vandeparre *et al*. [15], as noted after equation (1.2): wrinklons change the wrinkle number by an $O(1)$ amount and hence are shorter.

The effect of the parameter α on the wrinkle branching patterns is shown for some particular values in figure 6; a video illustrating how the equilibrium varies with α can be found in the electronic supplementary material. We observe a number of very different regimes as the dimensionless substrate stiffness gradient α in equation (3.13) varies. We see that for small α, the number of wrinkles varies gradually in space, with branching events spread out along 'defect lines'. Along these defect lines, the wrinkle amplitude is also lower than other portions of the sheet (figure 6*a*). As α increases, the stiffness gradient increases and so the number of wrinkles needs to change more rapidly. To achieve this, the branching events move closer together in x, and eventually align in the y-direction instead (figure 6*b–d*). For sufficiently large α, when the substrate gradient is very steep or tension is strong compared to residual stresses, the branching events all occur at the line $\bar{X}=0$, and the number of wrinkles simply jumps rapidly between the two far-field values (figure 6*d*). This perfect line of defects arises in part from assuming $\beta_n = 0$ in the reconstruction; if phase shifts could be determined we anticipate that the branching line might shift slightly across the sheet as shown, for example, in figure 3*a*.

[1]Note, however, that large α is *not* inconsistent with the assumption $|\lambda'| \ll 1$, which only requires that $\alpha\delta^2\lambda\sqrt{K/T} \ll 1$ and hence can be satisfied by sufficiently small δ and/or wavelength $\lambda\sqrt{K/T}$.

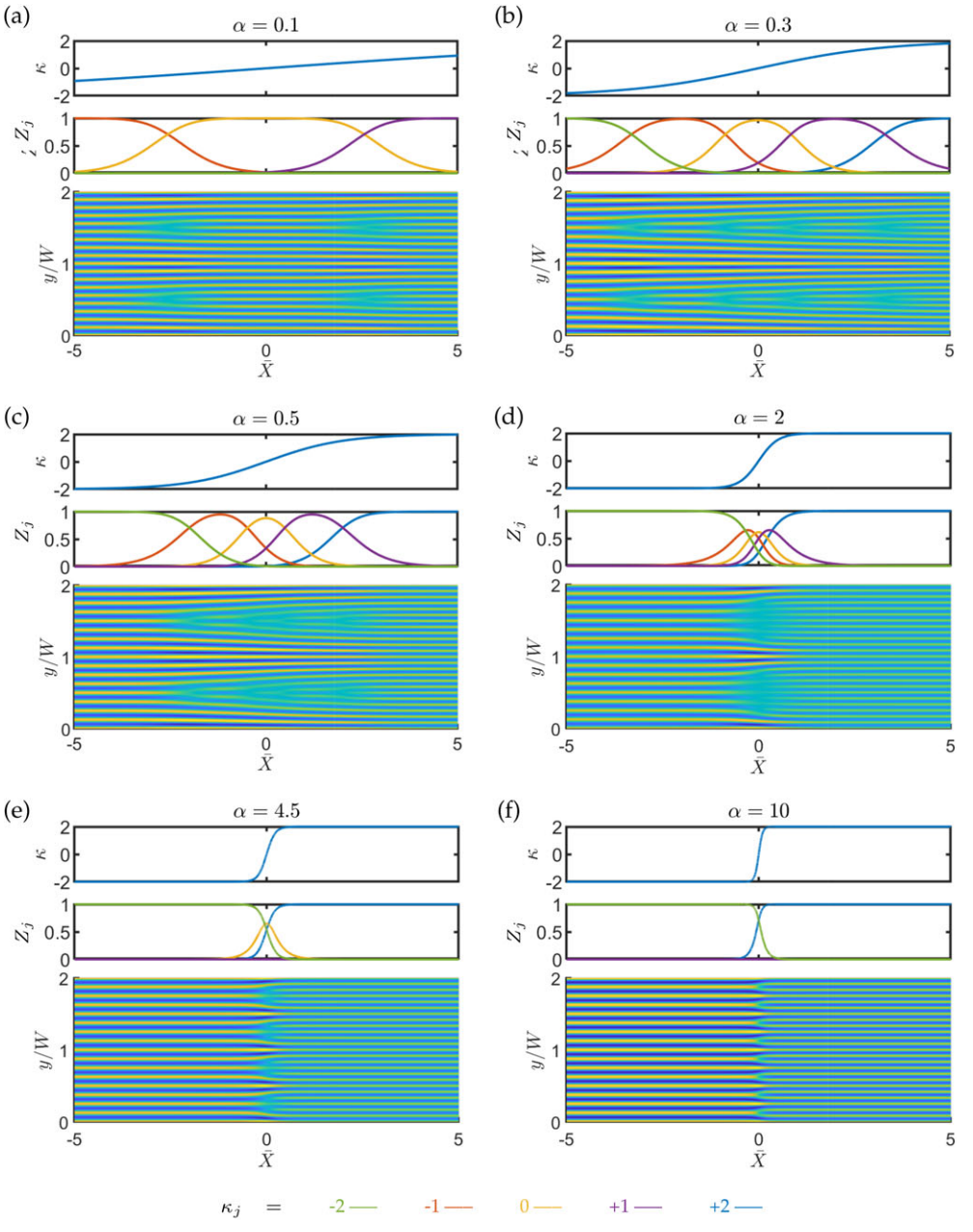

Figure 6. Wrinkle profiles in a sheet where the preferred number of wrinkles in the interval $0 \leq y/W \leq 1$ changes smoothly by 4. Different sub-figures show the effect of the dimensionless stiffness gradient, α, from $\alpha = 0.1$ to $\alpha = 10$. In each case, the top panel shows the stiffness gradient defined by equation (3.13), the middle panel shows the calculated spatial variation of the amplitude of each mode, as predicted by the solution of equation (3.9), and the bottom panel shows a reconstruction of the surface profile for the particular case in which the number of wrinkles in $y/W \in [0, 1]$ increases from 8 to 12. (The phase shifts β_n from equation (3.6) are not determined in our analysis; our reconstructed wrinkle profiles assume $\beta_n = 0$.) The line colours used in the middle panel indicates the mode number κ_j, as indicated at the base of the figure.

(c) Amplitude modulation

We conclude this section by using our Fourier series solution to gain some insight into the amplitude modulation effect visible in figures 3 and 6 and predicted previously by Tovkach

et al. [12]. For sufficiently shallow stiffness gradients (i.e. sufficiently small α in figure 6a–c), we observe that at the particular values of $\bar{X}$ where defects occur, there are just two adjacent wrinkle modes excited, say modes l and $l+1$. The length constraint (equation (3.9*b*)) then gives that $Z_l = Z_{l+1} = 1/\sqrt{2}$ and so the Fourier sum at this point can be written

$$\sum_j Z_j \sin\left(2\pi n_j \frac{y}{W}\right) = \frac{1}{\sqrt{2}}\left[\sin\left(2\pi n_l \frac{y}{W}\right) + \sin\left(2\pi (n_l+1)\frac{y}{W}\right)\right]$$
$$= \sqrt{2}\sin\left(2\pi \frac{y}{\bar{\lambda}}\right)\cos\left(\pi \frac{y}{W}\right) + O(\delta), \tag{3.15}$$

for some specific l. We can therefore interpret the surface profile as the product of a highly oscillatory part contributing the individual wrinkles and a slowly varying part controlling the overall amplitude. The slowly varying part, and therefore the product, is close to zero in the vicinity of $y = W/2, 3W/2, \ldots$, giving rise to the characteristic modulation pattern observed. Furthermore, the defect lines that emerge naturally in e.g. figure 6c just correspond to y-positions where two adjacent modes are exactly out of phase; from the first line of equation (3.15) this also occurs at $y = W/2, y = 3W/2, \ldots$.

For values of $\bar{X}$ in between defects, again for sufficiently small α, we observe three adjacent modes and write

$$\sum_j Z_j \sin\left(2\pi n_j \frac{y}{W}\right) = 2(Z_{l-1} + Z_{l+1})\sin\left(2\pi \frac{y}{\bar{\lambda}}\right)\cos\left(\pi \frac{y}{W}\right)$$
$$+ \left[\sqrt{1 - Z_{l-1}^2 - Z_{l+1}^2} - Z_{l-1} - Z_{l+1}\right]\sin\left(2\pi \frac{y}{\bar{\lambda}}\right) + O(\delta) \tag{3.16}$$

for the relevant integer l. In this case, we interpret the surface profile as the sum of a highly oscillatory part with amplitude modulation, as in equation (3.15), and another highly oscillatory part with uniform amplitude. We therefore expect to see some amplitude modulation between defects as well as at them, but that the strength of this modulation will depend on the size of the contribution from modes adjacent to the dominant one, and will disappear if there is a zone where only one mode is excited and $Z_{l-1} = Z_{l+1} = 0$; this happens for very small α as in figure 6a.

4. Qualitative experiments

Before seeking to better understand the transition between cascade-like and defect-like behaviour just observed, we would like to check whether the transition behaviour observed in our reduced numerical model can be observed experimentally. To test this, we performed experiments in which a thin elastic sheet (thickness $h = 60$ mm, Young's modulus $E = 800$ MPa, giving $B = 1.7 \times 10^{-5}$ N m^{-1}) was adhered to a substrate fabricated from polyvinylsiloxane (Zhermack). Previous experiments [27] have demonstrated that this solid is linear for strains $\lesssim 10\%$; it is also reasonable to assume the substrate is isotropic since it polymerizes from a liquid state. Nevertheless, to make a substrate thin enough that it behaves like a Winkler substrate would require [28] that $h_s \lesssim 1$ mm, which is not attainable in our laboratory. Instead, we use a deep substrate, $h_s \approx 5$ cm, in which case the wrinkle wavelength is [9,29]

$$\lambda \propto \left(\frac{E}{E_s}\right)^{1/3} h. \tag{4.1}$$

Given this important difference with the linear substrate, any comparison with the results of our theoretical analysis can only be qualitative. Nevertheless, substrates with different stiffness gradient were created by mixing differing ratios of catalyst and base; the resulting substrates had (local) stiffness in the range 80 kPa $\leq E_s \leq$ 720 kPa [30]. (This range of E_s is chosen to ensure that the preferred wavelength changes by a factor of more than 2 over the 10 cm length of the substrate, given the modified dependence on substrate stiffness in equation (4.1).) However, the stiffness gradient is changed between substrates, as indicated in the top portion of figure 7.

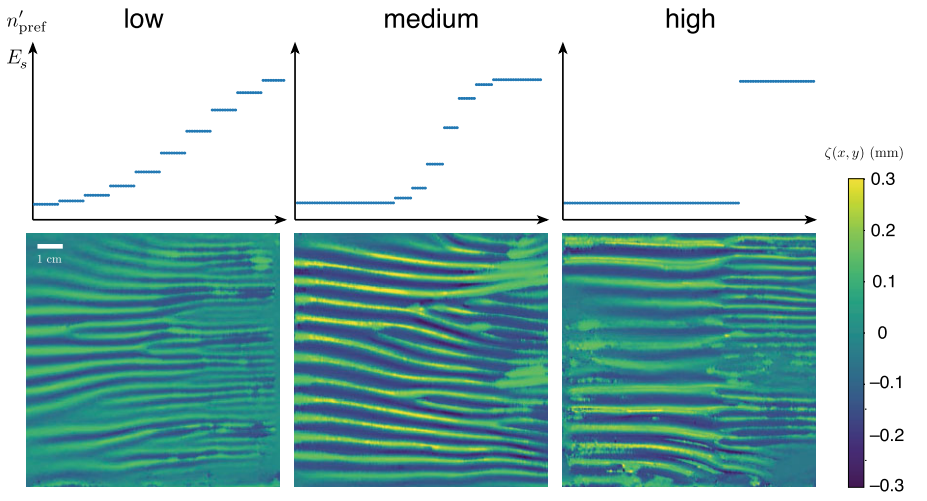

Figure 7. Experimentally obtained surface profiles for different levels of the substrate stiffness gradient, characterized in terms of the gradient in preferred wrinkle number, $n'_{\text{pref}}(x)$. Schematic illustrations of the different substrate stiffness profiles used in each of the three case are given in the top row, together with a qualitative measure of the size of $n'_{\text{pref}}(x)$. The images themselves show the three-dimensional surface profile in each case with the out-of-plane displacement (relative to the mean) given by the colour bar to the right. Despite the various caveats discussed in the main text, these profiles qualitatively display similar behaviour to our numerical results, namely that small gradients show wrinkle branching, while large gradients illustrate a cascade.

Another key difference between the system modelled here and this experiment is that no tension T is directly applied to the system.[2] Nevertheless, when compressed (using a micrometre screw gauge) between vertical walls, qualitatively different wrinkle patterns are observed depending on whether the stiffness changes suddenly or more gradually. The surface profiles are imaged by using several images of the wrinkled surface taken from different angles (see electronic supplementary material). The results of this analysis can be seen in figure 7, which shows that substrates with a more rapid change in the value of E_s do demonstrate a single generation cascade at the point where the substrate stiffness changes, while with a more gradual change, individual wrinkle branching events take place. Despite this qualitative similarity, we note that the defects are not all aligned, showing that the phases, β_n, do evolve, in addition to the wrinkle amplitude.

5. Bifurcation analysis

The rapid jump in wrinkle number for larger α is associated with the apparent loss of some Fourier modes from the solution. When α is sufficiently small and the stiffness gradient is sufficiently shallow, each of the five modes dominates the pattern at some point (i.e. for some interval in $\bar{X}$). However, as α increases the situation changes: when $\alpha = 4.5$ only three modes are excited and the dominant wavenumber transitions very rapidly between the two extreme values; when $\alpha = 10$ only the two extreme modes are excited, with a rapid transition between them.

The numerical results of figure 8 further suggest that close to the critical values of α at which these transitions occur, the size of the mode that is about to disappear exhibits a scaling law with the distance to threshold. For example, the $j = 0$ mode appears to disappear at $\alpha \approx 8$ (figure 8a, main figure) while, for $\alpha < 8$, the maximum amplitude of this mode $||Z_0||_\infty \propto (8 - \alpha)^{1/2}$ (see inset of figure 8a). A similar scaling behaviour is seen for the disappearance of the $j = \pm 1$ modes, with the critical value there being $\alpha \approx 4$ (data not shown). To understand the behaviour as α increases

[2] An effective tension may act on the sheet because of the substrate's expansion perpendicular to the imposed displacement—a result of the Poisson effect.

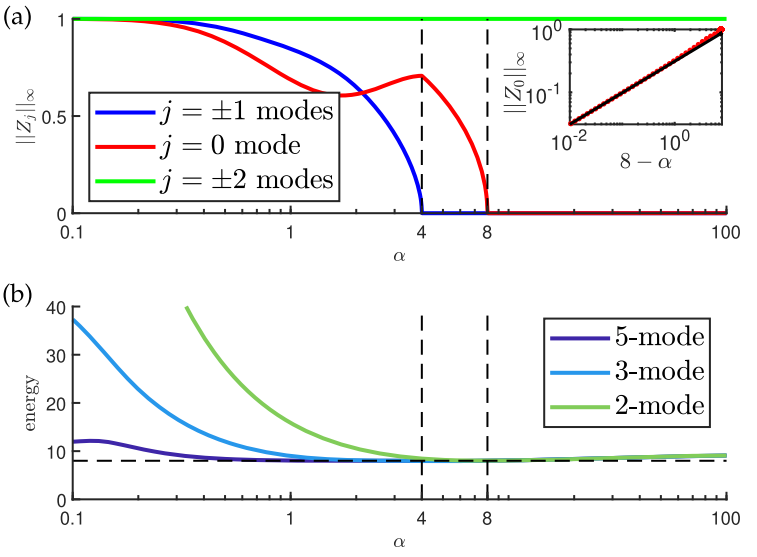

Figure 8. (a) Maximum amplitude of each of the modes, $||Z_j||_\infty = \max_{\bar{X}}\{Z_j\}$, in the five-mode problem, as the stiffness gradient α varies. Inset: decay of the amplitude of the last 'optional' mode, Z_0, near $\alpha = 8$. Red markers show the numerical solution and the black line shows the asymptotic solution, (5.13). (b) Energy of the degenerate solutions with 2, 3 and 5 non-zero Fourier modes as α varies.

better, we consider the apparent disappearance of the $j = 0$ mode at $\alpha \approx 8$ in more detail. We begin with a description of the full three-mode problem that is pertinent to this disappearance of a third mode.

(a) The full problem

We are interested in going from having $N - 2$ to $N + 2$ wrinkles with the key question being whether we will excite the mode with N wrinkles (this being an 'optional' third mode). We therefore let

$$Z_{-2} = \sin\theta\cos\phi, \quad Z_0 = \sin\phi, \quad Z_{+2} = \cos\phi\cos\theta \tag{5.1}$$

with the convention for ϕ chosen such that $\phi = 0$ corresponds to the N-wrinkle mode being omitted. The appropriate boundary conditions are:

$$\phi \to 0, \quad \text{as} \quad \bar{X} \to \pm\infty, \quad \theta(-\infty) = \frac{\pi}{2}, \quad \theta(+\infty) = 0. \tag{5.2}$$

Substituting this ansatz into the governing equations for each mode and eliminating $\bar{S}$, we find that

$$\frac{\mathrm{d}^2\phi}{\mathrm{d}\bar{X}^2} = -[16 + (\theta')^2 - 32(\tanh\alpha\bar{X})(\cos 2\theta)](\cos\phi)(\sin\phi) \tag{5.3}$$

and

$$\frac{\mathrm{d}^2\theta}{\mathrm{d}\bar{X}^2} = 2\theta'\phi'\tan\phi + 64(\tanh\alpha\bar{X})\cos\theta\sin\theta, \tag{5.4}$$

which are to be solved with boundary conditions (equation (5.2)).

(b) An analytical solution for $\alpha = 8$

The system of equations (5.2)–(5.4) can readily be solved numerically. As expected (based on the numerics with five modes) a change in behaviour is observed when $\alpha = 8$. In particular, as $\alpha \nearrow 8$,

the maximum amplitude of ϕ decreases appearing to vanish at $\alpha = 8$; for $\alpha \geq 8$, we are only able to find numerical solutions with $\phi = 0$.

To understand this behaviour, we begin by noting that when $\phi = 0$, the equation for θ in equation (5.4) simplifies considerably becoming:

$$\frac{\mathrm{d}^2(2\theta)}{\mathrm{d}\bar{X}^2} = 64\tanh(\alpha\bar{X})\sin 2\theta, \tag{5.5}$$

with boundary conditions $\theta \to \pi/2$ as $\bar{X} \to -\infty$ and $\theta \to 0$ as $\bar{X} \to \infty$. (Unsurprisingly, equation (5.5) is a particular case of the two-mode problem given in equation (3.11).)

In the particular case $\alpha = 8$, equation (5.5) with the appropriate boundary conditions has the exact solution

$$\theta(\bar{X}) = \tan^{-1}\left(e^{-8\bar{X}}\right) := \theta_8(\bar{X}). \tag{5.6}$$

Substituting this exact solution into the linearized version of equation (5.3) we find that

$$\phi(\bar{X}) = A\,\mathrm{sech}^{1/2}(8\bar{X}) := \phi_8(\bar{X}), \tag{5.7}$$

where the amplitude A is arbitrary—since equation (5.3) was linearized to make progress, its solution may be arbitrarily scaled. To determine this amplitude, and in particular how the solution behaves for $0 < 8 - \alpha = \epsilon \ll 1$, we use a weakly nonlinear analysis.

(c) Weakly nonlinear analysis

We begin by letting

$$\epsilon = 8 - \alpha \ll 1 \tag{5.8}$$

and pose a power series for the functions $\theta(\bar{X})$ and $\phi(\bar{X})$ of the form

$$\theta(\bar{X}) = \theta_8(\bar{X}) + \epsilon\Theta(\bar{X}) + \cdots \tag{5.9}$$

and

$$\phi(\bar{X}) = \epsilon^{1/2}\phi_8(\bar{X}) + \epsilon^{3/2}\Phi(\bar{X}) + \cdots, \tag{5.10}$$

where $\theta_8(\bar{X})$ and $\phi_8(\bar{X})$ are as defined in equations (5.6) and (5.7), respectively. Here, we note that the appearance of powers of $\epsilon^{1/2}$ in the expansion for $\phi(\bar{X})$ is motivated by the quadratic nonlinearity in ϕ of the equation for θ, equation (5.4): for these terms to balance with the change to the potential, $\tanh\alpha\bar{X} = \tanh 8\bar{X} - \epsilon\,\mathrm{sech}^2 8\bar{X} + O(\epsilon^2)$, we require the size of $\phi(\bar{X})$ to be $O(\epsilon^{1/2})$; this is consistent with our numerical results also (see inset of figure 8).

Substituting the series solutions from equations (5.9) and (5.10) into equations (5.3) and (5.4), we find the coupled linear equations

$$\frac{\mathrm{d}^2\Theta}{\mathrm{d}\bar{X}^2} - 64(\tanh^2 8\bar{X})\Theta = -32\bar{X}\mathrm{sech}^3 8\bar{X} + 16\pi A^2\mathrm{sech}^2 8\bar{X}\tanh 8\bar{X} \tag{5.11}$$

and

$$\begin{aligned}\frac{\mathrm{d}^2\Phi}{\mathrm{d}\bar{X}^2} - 16(1 - 3\mathrm{sech}^2 8\bar{X})\,\Phi = &-\frac{32A^3}{3}(1 - 3\mathrm{sech}^2 8\bar{X})\phi_8^3 \\ &- 8A\,\phi_8\,\mathrm{sech}8\bar{X}\left[4\bar{X}\tanh 8\bar{X}\mathrm{sech}8\bar{X} + 8\Theta\tanh 8\bar{X} - \frac{\mathrm{d}\Theta}{\mathrm{d}\bar{X}}\right].\end{aligned} \tag{5.12}$$

The system (equations (5.11)–(5.12)) is a linear system for the functions Θ and Φ with homogeneous boundary conditions. According to the Fredholm Alternative Theorem [31], it therefore has non-trivial solutions only if the forcing (RHS) is orthogonal to the solution of the homogeneous adjoint problem. Numerical solution of the associated homogeneous adjoint problem (and calculation of the associated solvability condition) gives that we must have $A \approx 0.248$. (Details of this calculation are given in the electronic supplementary material.)

We therefore have that

$$||Z_0||_\infty = ||\phi_8(\bar{X})||_\infty \sim 0.248\sqrt{\frac{\pi}{2}}\sqrt{8-\alpha} \tag{5.13}$$

as $\alpha \to 8$. This prediction is represented by the solid line in the inset of figure 8a, and agrees well with the numerical results presented there also.

Finally, we also note that multiple solutions exist for $\alpha < 8$: for $4 < \alpha < 8$, it is possible to find solutions with both three-modes and two-modes. However, the two-mode solution is energetically more expensive (and hence unfavourable) than the three-mode solution. Similarly, for $0 < \alpha < 4$, solutions exist with five, three or two modes. The energetically favoured solution has five modes. This energetic structure is summarized in figure 8b; crucially only the two-mode solution exists for $\alpha > 8$.

6. Discussion

In this paper, we have presented a study of how wrinkle patterns adapt to a preferred (locally energy minimizing) wrinkle wavelength that evolves spatially. This study was motivated by experimental observations that suggest changes in this preferred wrinkle number can be accommodated either by adding one wrinkle at a time at particular points within the pattern (termed 'wrinkle branching') or by each wrinkle bifurcating to instantly double the number of wrinkles formed (a 'cascade'). Surface Evolver simulations confirmed the existence of wrinkle branching as a distinct regime and showed that the dominant wavelength is generally close to the locally preferred one. These simulations also showed that the polychromatic nature of the wrinkle pattern (how many different wavelengths are excited at a given position) depends on the steepness of the stiffness gradient: at low gradients the patterns are largely monochromatic with the neighbouring mode excited only as the transition between neighbouring modes occurs. This might be considered to be archetypal of wrinkle branching: wrinkles are added one at a time, with only one wavelength dominating the pattern at any given position. At moderate gradients, multiple modes are excited in the neighbourhood of the transition: the wrinkle pattern is poly-chromatic in the neighbourhood of the transition for steep gradients.

We also used a simplified model to study the evolution of the amplitude of each wrinkle mode. With this model, we replicated the increased polychromaticity of wrinkle patterns as the stiffness gradient increases from low to moderate values. Moreover, this model generated spatially varying wrinkle spectra that are qualitatively similar to Surface Evolver simulations. We also showed that at high stiffness gradients, intermediate modes may not be excited at all. We suggest that this 'mode skipping' is a precursor of the cascade that is often observed experimentally. Our simplified model introduces a measure of stiffness gradient—the parameter α defined in equation (3.14)—that also incorporates the role of the applied tension. We show that the transition to mode skipping occurs at a critical value of α and show that the amplitude of the disappearing modes exhibits critical behaviour, determining the relevant critical exponent. However, we emphasize that the calculated critical value, $\alpha_c = 8$, depends on the stiffness profile assumed in equation (3.13). If curvature along the wrinkles were introduced, we would expect this to have a similar effect to decreasing the tension or stiffening the substrate (i.e. to decreasing α), but we have not explored that scenario in the current work.

Our simulations and simplified model also revealed that in the region where wrinkle branching events take place the overall amplitude is decreased. This is consistent with what was reported by Tovkach *et al.* [12] for the situation where changes in wrinkle number are required because of geometric (in)compatability. Our simplified model uses a Fourier decomposition and allows this amplitude suppression to be interpreted as a beating phenomenon: a collection of Fourier modes interfere destructively in the neighbourhood of a branching event. This amplitude suppression may also have practical implications. For example, amplitude suppression in some parts of a wrinkle pattern, combined with the inextensibility constraint, necessarily means that the

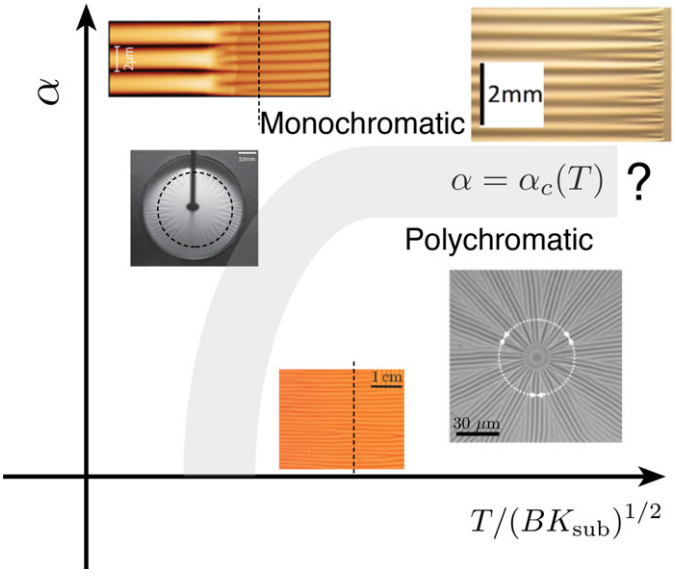

Figure 9. Schematic representation of what the regime diagram might look like. Experimental images used here are reproduced from papers with permission, as in figure 1. We hypothesize that there is curve in this regime-diagram (grey curve) that separates wrinkle branching (which is polychromatic) from cascades (which is monochromatic). The limit considered here corresponds to a transition at $\alpha = 8$ as $T/\sqrt{BK_{\text{sub}}} \gg 1$.

wrinkle amplitude is elevated elsewhere; this may have consequences for the global compressive strain at which failure mechanisms like delamination [27] and fracture [32] are observed.

More broadly, the analysis presented here could be adapted to circular or annular geometries where spoke-like wrinkles arise from azimuthal compression. In those geometries, fixing the wavelength will require the number of wrinkles to increase with radial position, so branching can occur even for uniform substrates. In a similar fashion to the system studied here, the observed branching behaviour will depend on factors such as applied tension and substrate stiffness.

Our analysis focused on the limit of large tension to simplify the amplitude evolution equations. We hypothesize that the behaviour we have explored in this paper is therefore one axis (α) of a larger, at least two-dimensional, parameter space, $(T/\sqrt{BK_{\text{sub}}}, \alpha)$. It is well known that smooth wrinkle branching can only be expected for $T \gtrapprox \sqrt{BK_{\text{sub}}}$, with sharper fold-like behaviour expected below this threshold [23]. A sketch of the possible regime diagram is shown in figure 9. (Note that for certain wrinkle number profiles (3.13)—for example, for different values of α or larger maximum change in $n_{\text{pref}} - n_* > 4$—the system may be below the classical wrinkle-to-fold threshold at the soft end of the substrate but above the threshold at the stiff end of the substrate. In this case, it is feasible that a sheet may exhibit a mixture of polychromatic wrinkles and folds, and possibly even fold branching, making the hypothetical regime diagram more complex. However, given that the folding phenomenology is rich even in the absence of substrate gradients [22], it is difficult to anticipate the exact behaviour without further study.)

We finish by noting that our Surface Evolver simulations were consistent with the theoretical picture we have laid out above, but did not explicitly observe mode skipping or a cascade. We believe that this is because the simulations were not able to reach sufficiently large values of the dimensionless stiffness gradient α. Our simulations were constrained by the requirement that the induced displacement is large enough to exceed the wrinkle threshold throughout the sheet, but also small enough to avoid the development of folds [33]. More details of the effect of this restriction on our simulations are given in the electronic supplementary material but essentially resolving this would require a much smaller value of $K_{\max}L/(Eh)$, which is most likely to be achieved with a higher value of the stretching modulus Eh, which brings with it other difficulties,

including additional computational cost. At the same time, the experimental literature is replete with examples of this mode-skipping/cascade, and it is the wrinkle branching that seems to be observed only rarely. We therefore encourage experiments in which wrinkle branching might be observed and studied in more detail using a substrate stiffness that varies only slowly.

Data accessibility. The data used to generate the figures in this paper is publicly available via the Oxford Research Archive via [34].

Additional data, and further details of the analysis, are provided in electronic supplementary material [35].

Declaration of AI use. We have not used AI-assisted technologies in creating this article.

Authors' contributions. D.O.: conceptualization, formal analysis, investigation, software, writing—original draft, writing—review and editing; M.X.: formal analysis, software, writing—original draft; P.L.: formal analysis, methodology, writing—review and editing; D.V.: conceptualization, formal analysis, funding acquisition, methodology, project administration, supervision, writing—original draft, writing—review and editing.

All authors gave final approval for publication and agreed to be held accountable for the work performed therein.

Conflict of interest declaration. We declare we have no competing interests.

Funding. The research leading to these results has received funding from Research Ireland under the Frontiers for the Future Programme, grant no. 21/FFP-P/10160 (D.O.K.), and from the European Research Council under the European Union's Horizon 2020 Programme/ERC grant no. 637334 and the Leverhulme Trust (D.V.).

Acknowledgements. The authors would also like to acknowledge conversations with Benny Davidovitch and Jon Chapman. For the purpose of Open Access, the authors will apply a CC BY public copyright license to any Author Accepted Manuscript version arising from this submission.

References

1. Kim JB, Kim P, Pégard NC, Oh SJ, Kagan CR, Fleischer JW, Stone HA, Loo Y-L. 2012 Wrinkles and deep folds as photonic structures in photovoltaics. *Nat. Photon.* **6**, 327–332. (doi:10.1038/nphoton.2012.70)
2. Harrison C, Stafford CM, Zhang W, Karim A. 2004 Sinusoidal phase grating created by a tunably buckled surface. *Appl. Phys. Lett.* **85**, 4016–4018. (doi:10.1063/1.1809281)
3. Cerda E, Mahadevan L. 2003 Geometry and physics of wrinkling. *Phys. Rev. Lett.* **90**, 074302. (doi:10.1103/PhysRevLett.90.074302)
4. Davidovitch B, Schroll RD, Vella D, Adda-Bedia M, Cerda EA. 2011 Prototypical model for tensional wrinkling in thin sheets. *Proc. Natl Acad. Sci. USA* **108**, 18 227–18 232. (doi:10.1073/pnas.1108553108)
5. Reis PM. 2015 A perspective on the revival of structural (in) stability with novel opportunities for function: from buckliphobia to buckliphilia. *J. Appl. Mech.* **82**, 111001. (doi:10.1115/1.4031456)
6. Taffetani M, Vella D. 2017 Regimes of wrinkling in pressurized elastic shells. *Phil. Trans. R. Soc. A* **375**, 20160330. (doi:10.1098/rsta.2016.0330)
7. Paulsen JD, Hohlfeld E, King H, Huang J, Qiu Z, Russell TP, Menon N, Vella D, Davidovitch B. 2016 Curvature-induced stiffness and the spatial variation of wavelength in wrinkled sheets. *Proc. Natl Acad. Sci. USA* **113**, 1144–1149. (doi:10.1073/pnas.1521520113)
8. Hohlfeld E, Davidovitch B. 2015 Sheet on a deformable sphere: wrinkle patterns suppress curvature-induced delamination. *Phys. Rev. E* **91**, 012407. (doi:10.1103/PhysRevE.91.012407)
9. Stafford CM *et al*. 2004 A buckling-based metrology for measuring the elastic moduli of polymeric thin films. *Nature Mat.* **3**, 545–550. (doi:10.1038/nmat1175)
10. Vella D, Davidovitch B. 2018 Regimes of wrinkling in an indented floating elastic sheet. *Phys. Rev. E* **98**, 013003. (doi:10.1103/PhysRevE.98.013003)
11. Vella D, Huang J, Menon N, Russell TP, Davidovitch B. 2015 Indentation of ultrathin elastic films and the emergence of asymptotic isometry. *Phys. Rev. Lett.* **114**, 014301. (doi:10.1103/PhysRevLett.114.014301)
12. Tovkach O, Chen J, Ripp MM, Zhang T, Paulsen JD, Davidovitch B. 2020 Mesoscale structure of wrinkle patterns and defect-proliferated liquid crystalline phases. *Proc. Natl Acad. Sci. USA* **117**, 3938–3943. (doi:10.1073/pnas.1916221117)
13. Davidovitch B. 2009 Period fissioning and other instabilities of stressed elastic membranes. *Phys. Rev. E* **80**, 025202. (doi:10.1103/PhysRevE.80.025202)

14. Schroll RD, Katifori E, Davidovitch B. 2011 Elastic building blocks for confined sheets. *Phys. Rev. Lett.* **106**, 074301. (doi:10.1103/PhysRevLett.106.074301)
15. Vandeparre H *et al*. 2011 Wrinkling hierarchy in constrained thin sheets from suspended graphene to curtains. *Phys. Rev. Lett.* **106**, 224301. (doi:10.1103/PhysRevLett.106.224301)
16. Knapp A, Nebel LJ, Nitschke M, Sander O, Fery A. 2021 Controlling line defects in wrinkling: a pathway towards hierarchical wrinkling structures. *Soft Matter* **17**, 5384–5392. (doi:10.1039/D0SM02231D)
17. Huang J, Davidovitch B, Santangelo CD, Russell TP, Menon N. 2010 Smooth cascade of wrinkles at the edge of a floating elastic film. *Phys. Rev. Lett.* **105**, 038302. (doi:10.1103/PhysRevLett.105.038302)
18. Hure J, Roman B, Bico J. 2012 Stamping and wrinkling of elastic plates. *Phys. Rev. Lett.* **109**, 054302. (doi:10.1103/PhysRevLett.109.054302)
19. Schleifer J, Marthelot J, Jones TJ, Brun P-T. 2019 The fingerprint of a flow: wrinkle patterns in nonuniform coatings on pre-stretched soft foundations. *Soft Matter* **15**, 1405–1412. (doi:10.1039/C8SM02057D)
20. Chung JY, Nolte AJ, Stafford CM. 2009 Diffusion-controlled, self-organized growth of symmetric wrinkling patterns. *Adv. Mater.* **21**, 1358–1362. (doi:10.1002/adma.200803209)
21. Vandeparre H, Gabriele S, Brau F, Gay C, Parker KK, Damman P. 2010 Hierarchical wrinkling patterns. *Soft Matter* **6**, 5751–5756. (doi:10.1039/c0sm00394h)
22. Gordillo L, Knobloch E. 2019 Fluid-supported elastic sheet under compression: multifold solutions. *Phys. Rev. E* **99**, 043001. (doi:10.1103/PhysRevE.99.043001)
23. Pomeau Y. 1998 Buckling of thin plates in the weakly and strongly nonlinear regimes. *Phil. Mag. B* **78**, 235–242. (doi:10.1080/13642819808202946)
24. Brakke K. 1992 The surface evolver. *Exp. Math.* **1**, 141–165. (doi:10.1080/10586458.1992.10504253)
25. Xin M. 2021 *Deformations of geometrically frustrated elastic sheets*. PhD thesis, University of Massachusetts Amherst.
26. Blumenson LE. 1960 A derivation of n-dimensional spherical coordinates. *Amer. Math. Mon.* **67**, 63–66. (doi:10.2307/2308932)
27. Vella D, Bico J, Boudaoud A, Roman B, Reis PM. 2009 The macroscopic delamination of thin films from elastic substrates. *Proc. Natl Acad. Sci. USA* **106**, 10 901–10 906. (doi:10.1073/pnas.0902160106)
28. Genzer J, Groenewold J. 2006 Soft matter with hard skin: from skin wrinkles to templating and material characterization. *Soft Matter* **2**, 310–323. (doi:10.1039/b516741h)
29. Allen HG. 1969 *Analysis and design of structural sandwich panels*. Oxford, UK: Pergamon Press.
30. Box F, Jaquemot C, Adda-Bedia M, Vella D. 2020 Cloaking by coating: how effectively does a thin, stiff coating hide a soft substrate? *Soft Matter* **16**, 4574–4583. (doi:10.1039/C9SM02511A)
31. Keener JP. 1988 *Principles of applied mathematics*. Redwood City, CA: Addison-Wesley.
32. Mei H, Huang R, Chung JY, Stafford CM, Yu H-H. 2007 Buckling modes of elastic thin films on elastic substrates. *Appl. Phys. Lett.* **90**, 151902. (doi:10.1063/1.2720759)
33. Oshri O, Brau F, Diamant H. 2015 Wrinkles and folds in a fluid-supported sheet of finite size. *Phys. Rev. E* **91**, 052408. (doi:10.1103/PhysRevE.91.052408)
34. Vella D, O'Kiely D. 2025 *Wrinkling of a bilayer with spatially-varying stiffness: from wrinkle branching to cascades*. Oxford, UK: University of Oxford. (doi:10.5287/ora-gjmy25ake)
35. O'Kiely D, Xin M, Lecointre P, Vella D. 2025 Wrinkling of a bilayer with spatially varying stiffness: from wrinkle branching to cascades. Figshare. (doi:10.6084/m9.figshare.c.7834474)